

Designing single-beam multitraping acoustical tweezers

Glauber T. Silva¹ and André L. Baggio

Physical Acoustics Group, Instituto de Física, Universidade Federal de Alagoas, Maceió, AL 57072-970, Brazil.

Abstract

The concept of a single-beam acoustical tweezer device which can simultaneously trap microparticles at different points is proposed and demonstrated through computational simulations. The device employs an ultrasound beam produced by a circular focused transducer operating at 1 MHz in water medium. The ultrasound beam exerts a radiation force that may tweeze suspended microparticles in the medium. Simulations show that the acoustical tweezer can simultaneously trap microparticles in the pre-focal zone along the beam axis, i.e. between the transducer surface and its geometric focus. As acoustical tweezers are fast becoming a key instrument in microparticle handling, the development of acoustic multitraping concept may turn into a useful tool in engineering these devices.

Keywords: Acoustical Tweezer, Acoustic Radiation Force, Ultrasound Focused Beam

1. Introduction

Noncontact particle handling methods based on optical [1] and acoustic [2] radiation forces are promoting a revolution in biotechnology and biomedical applications [3, 4, 5, 6, 7]. Techniques for particle trapping which employ a laser and an ultrasound beam are known, respectively, as optical tweezer [8] and acoustical tweezer [9]. Methods based on acoustical tweezers are potentially useful in applications for which optical tweezers can hardly operate. For instance, handling particles in opaque medium to electromagnetic radiation cannot be performed by optical tweezers. Furthermore, a laser beam may damage biological structures by heating and also by a process called photodamage, which is related to the formation of singlet oxygen when photon absorption occurs [10].

Two different approaches have been employed to acoustically trap microparticles, namely standing waves and single-beam methods. The first acoustical tweezer device used two counterpropagating focused ultrasound beams to form a standing wave at 3.5 MHz, which was used to trap 270 μm -diameter latex particles and frog eggs in water [9]. In other arrangement, an ultrasound standing wave generated between a 2.1 MHz linear array and a reflector trapped alumina microparticles with 16 μm mean diameter [11]. Devices in the acoustofluidics realm are, in general, based on standing waves [12, 13]. Standing surface acoustic waves (SSAW) have been used to trap particles with diameter smaller than 8 μm suspended in microfluidic channels [14, 15]. Standing Bessel waves were generated by a circular 64-element ultrasonic array to manipulate 90 μm -diameter polystyrene microparticles in 2D [16]. Tilted standing waves produced by a three PZT transducer setup which operated at 1.67 MHz were used to trap and transport a 100 μm -diameter silica bead [17]. Furthermore, the standing

wave method has been also employed to levitate particles and droplets in air [18, 19].

On the other hand, single-beam acoustical tweezers utilize tightly focused transducers and linear arrays for trapping microparticles in the device focus point. In particular, a 30 MHz-transducer with an f-number of 0.75 tweezed a 126 μm -diameter lipid microdroplet [20]. Higher frequency transducers operating at 200 MHz have been designed to handle a 10 μm -diameter leukemia cell [21] and microsphere [22]. A PZT transducer equipped with a multi-foci Fresnel lens generated a 17.9 MHz zeroth-order Bessel beam, which was employed to trap microspheres ranging in diameter from 70 to 90 μm [23]. A 57.5 MHz needle hydrophone with an f-number of 1 produced an ultrasound beam which tweezed a 30 μm diameter lipid microdroplet [24]. Also, a 64-element linear phased array operating at 26 MHz was able to trap a 45 μm -diameter polystyrene microparticle [25].

The key aspect in designing single-beam acoustical tweezers is how to form a beam to trap a particle with an specific size. Different schemes of acoustical tweezer beamforming have been previously investigated for a circular focused [26, 27, 28] and a linear array [29] transducer. In these studies, only one trapping point located in the transducer focal zone was considered. Recently, the possibility of trapping a particle in the nearfield of piezoelectric disk was discussed [30]. Perhaps the most serious disadvantage of this method is that the yielded ultrasound beam behaves like a plane progressive wave in the vicinity of the beam axis at the nearfield [31]. Hence, the transverse radiation force associated to the beam may not be strong enough to hold a particle in 3D. In this work, a method to form multiple microparticle traps in the pre-focal region of a piezoelectric focused transducer is proposed. The method's ability to tweeze microparticles is theoretically demonstrated through computational simulations. In so doing, the radiation force produced by a 1 MHz piezoelectric transducer, with focus at 50 mm

*Corresponding author: glauber@pq.cnpq.br

and an f-number of 1.25, which is readily available commercially, is computed on a microdroplet, made of either benzene or peanut oil, suspended in water. For this transducer configuration, trapping points arise in the pre-focal zone. After obtaining the radiation force field, the dynamics of the microparticle trapping is simulated considering effects of gravity, buoyancy and Stokes' drag. The results show that microparticle entrapment occurs in points as close as one third of the transducer focal distance.

2. Ultrasound beamforming

Before calculating the acoustic radiation force exerted on a particle, we need to establish the ultrasound beamforming by the focused transducer. Hence, consider a circular focused transducer, with aperture $2b$ and curvature radius z_0 , mounted on a compliant baffled at $z = 0$ (see Fig. 1). The transducer is immersed in an inviscid fluid of density ρ_0 and speed of sound c_0 and is uniformly excited with a sinusoidal signal of angular frequency ω . Thus, the ultrasound beam produced by the transducer is a time-harmonic wave described by its pressure $p_{\text{in}}(\mathbf{r})e^{-i\omega t}$ and velocity of a fluid parcel $\mathbf{v}_{\text{in}}(\mathbf{r})e^{-i\omega t}$, both observed at the time t in the position \mathbf{r} in a fixed coordinate system. Hereafter, the time-harmonic term $e^{-i\omega t}$ will be suppressed for the sake of simplicity. A useful pressure-velocity relation in first-order approximation is obtained from the momentum conservation equation as follows [32]

$$\mathbf{v}_{\text{in}} = -\frac{i}{\rho_0 c_0 k} \nabla p_{\text{in}}, \quad (1)$$

where $k = \omega/c_0$.

It is further assumed that the transducer concavity is fairly small and the wavelength is much smaller than its radius. Hence the ultrasound beam can be described in the paraxial approximation. In terms of the transducer parameter, these assumptions read [34]

$$\frac{1}{8N^2} \ll 1 \text{ and } 1 \ll kb \ll 128\pi N^3, \quad (2)$$

where $N = z_0/(2b)$ is the transducer f-number. The model discussed here may not be suitable for transducers with $N < 1$. On that account a different beamforming model might be considered [35].

By assuming that the transducer generates an axisymmetric paraxial beam, the pressure field can be expressed in cylindrical coordinates (ϱ, z) as

$$p_{\text{in}}(\varrho, z) = -i\rho_0 c_0 k e^{ikz} q(\varrho, z), \quad (3)$$

where q is the velocity potential characteristic function. For a circular focused transducer mounted on a perfectly compliant baffle at $z = 0$, one can show that the characteristic velocity

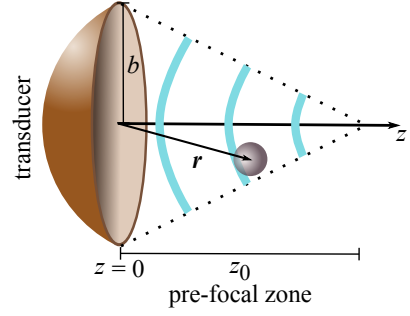


Figure 1: (Color online) Circular focused ultrasound transducer with aperture $2b$ and focus z_0 actuating on a spherical particle of radius a located at \mathbf{r} in the medium.

potential is given by [34]

$$q(\varrho, z) = \frac{v_0}{z} \exp\left(\frac{ik\varrho^2}{2z}\right) \int_0^b \exp\left[\frac{ik\varrho'^2}{2}\left(\frac{1}{z} - \frac{1}{z_0}\right)\right] \times J_0\left(\frac{k\varrho\varrho'}{z}\right) \varrho' d\varrho'. \quad (4)$$

where v_0 is the magnitude of the normal vibration velocity on the transducer surface, and J_m is the m th-order Bessel function. In the focal plane $z = z_0$, Eq. (4) becomes

$$q(\varrho, z_0) = -bv_0 \frac{J_1(kb\varrho/z_0)}{k\varrho}. \quad (5)$$

In the paraxial approximation, it follows from Eq. (1) and (3) that the fluid velocity is

$$\mathbf{v}_{\text{in}} \approx -\left[(\partial_\varrho q)\mathbf{e}_\varrho + ikq\mathbf{e}_z\right] e^{ikz}, \quad (6)$$

where \mathbf{e}_ϱ and \mathbf{e}_z are the unit-vector along the radial direction and z -axis. Here we are using the shorthand notation $\partial_\varrho = \partial/\partial\varrho$ and $\partial_z = \partial/\partial z$. Note that in deriving Eq. (6), we have neglected the term $\partial_z q$, because $|\partial_z q| \ll k|q|$. This assumption is valid in a region not very near to the transducer surface, say $z > 0.3z_0$.

3. Radiation force on a Rayleigh particle

Our attention now turns to the acoustic radiation force exerted by the ultrasound beam on a particle much smaller than the wavelength, i.e. the so-called Rayleigh regime. The particle has radius a , density ρ_1 , speed of sound c_1 , and its position is denoted by \mathbf{r} . Viscous effects of the host fluid in the radiation force analysis are neglected. This hypothesis holds when the external viscous boundary layer of the particle [32] $\delta_0 = \sqrt{2\nu_0/\omega}$ is much smaller than the particle radius, where ν_0 is the kinematic viscosity of the host fluid.

Using the radiation force formulas in Cartesian coordinates given in Ref. [36], one can show that the acoustic radiation force \mathbf{F}^{rad} on the Rayleigh particle is the sum of three components [37], namely the gradient \mathbf{F}^{grad} , the scattering \mathbf{F}^{sca} , and the absorption \mathbf{F}^{abs} radiation forces. Thus, we have

$$\mathbf{F}^{\text{rad}} = \mathbf{F}^{\text{grad}} + \mathbf{F}^{\text{sca}} + \mathbf{F}^{\text{abs}}. \quad (7)$$

The gradient radiation force is given by [38]

$$\mathbf{F}^{\text{grad}}(\mathbf{r}) = -\nabla U^{\text{rad}}(\mathbf{r}), \quad (8)$$

where

$$U^{\text{rad}} = \pi a^3 \left(f_0 \frac{|p_{\text{in}}|^2}{3\rho_0 c_0^2} - f_1 \frac{\rho_0 |v_{\text{in}}|^2}{2} \right) \quad (9)$$

is the radiation force potential energy. The quantities $f_0 = 1 - \rho_0 c_0^2/(\rho_1 c_1^2)$ and $f_1 = 2(\rho_1 - \rho_0)/(2\rho_1 + \rho_0)$ are the compressibility and density contrast factors of the particle, respectively. The gradient radiation force appears due to the interference between the incident and the scattered waves. Moreover, this force is responsible for trapping particles at the minima of the potential energy U^{rad} .

The scattering radiation force is given by [37]

$$\mathbf{F}^{\text{sca}}(\mathbf{r}) = \pi a^2 (ka)^4 \left[\frac{4}{9} \left(f_0^2 + f_0 f_1 + \frac{3f_1^2}{4} \right) \frac{\bar{\mathbf{I}}(\mathbf{r})}{c_0} - \frac{f_1^2}{6k} \text{Im}[\nabla \cdot \rho_0 \mathbf{v}_{\text{in}} \mathbf{v}_{\text{in}}^*(\mathbf{r})] \right], \quad (10)$$

where $\bar{\mathbf{I}} = (1/2)\text{Re}[p_{\text{in}} \mathbf{v}_{\text{in}}^*]$ is the incident intensity averaged in time and $\rho_0 \mathbf{v}_{\text{in}} \mathbf{v}_{\text{in}}^*$ is a dyadic (second-rank tensor).

The absorption radiation force reads [37]

$$\mathbf{F}^{\text{abs}}(\mathbf{r}) = \pi a^2 \tilde{\alpha}_1 ka \left[\frac{8(1 - f_0)}{3} \frac{\bar{\mathbf{I}}(\mathbf{r})}{c_0} - \frac{12(1 - f_0)}{5(\tilde{\rho}_1^{-1} + 2)^2} (ka)^2 \times \frac{1}{k} \text{Im}[\nabla \cdot \rho_0 \mathbf{v}_{\text{in}} \mathbf{v}_{\text{in}}^*(\mathbf{r})] \right], \quad (11)$$

where $\tilde{\rho}_1 = \rho_1/\rho_0$ and $\tilde{\alpha}_1 = \alpha_1(\omega/2\pi)^2/k_1$ is the normalized absorption of the particle, with α_1 being the absorption coefficient and $k_1 = \omega/c_1$. This equation is valid when absorption inside the particle is described through the dispersion relation

$$\kappa_1 = k_1(1 + i\tilde{\alpha}_1). \quad (12)$$

Furthermore, we also assume that the inner viscous boundary layer [39] $\delta_1 = \sqrt{2\nu_1/\omega}$ is much smaller than the particle radius, where ν_1 is the kinematic viscosity of the particle.

The absorption and the scattering radiation forces are only relevant when the beam has a traveling part, i.e. it locally behaves as a traveling plane wave. In the focal region, the acoustic beam has a traveling part. Thus, in principle, all three components of the radiation force in the focal region have to be taken into account. Both absorption and scattering radiation force point to the forward beam propagation direction. Obviously, these components tend to break the axial trapping stability.

The contribution of the momentum flux divergence $\text{Im}[\nabla \cdot \rho_0 \mathbf{v}_{\text{in}} \mathbf{v}_{\text{in}}^*]$ and the time-averaged intensity $\bar{\mathbf{I}}$ depend on the incident beam. In Appendix A, expressions of these two quantities are derived in the axial direction for a focused ultrasound beam in the paraxial approximation. In this case, we anticipate that for the transducer parameters which will be considered later, the contribution of the momentum flux divergence to the absorption and scattering radiation forces is much smaller than that due to

the averaged intensity.

In the focal plane, a particle might be trapped in $\varrho = 0$ if $\partial_{\varrho}^2 U^{\text{rad}}(0, z_0) > 0$. Using Eqs. (3), (5) and (6) into Eq. (9), one can show that this condition is satisfied when

$$f_0 < -\frac{3(k^2 b^4 + 64z_0^2)}{8(kbz_0)^2} f_1 \approx -\frac{3f_1}{32N^2}. \quad (13)$$

If the particle is denser than the host fluid ($\rho_1 > \rho_0$), then $0 \leq f_1 \leq 1$. Thus, to have a stable trap in the transducer focus it is necessary that $f_0 < 0$ which means that the particle should be less compressible than the host fluid. Yet not proven here, this behavior has been observed in the radiation force computed in the transducer pre-focal zone.

After obtaining the radiation force, one cannot assure that the possible trapping points are stable. In fact, entrapment also depends on gravity, buoyancy, and Stokes' drag acting on the microdroplet. Assume that gravity and buoyancy lies along the y-axis. Thus, the effective energy potential on the particle is given by

$$U^{\text{eff}} = U^{\text{rad}} + \frac{4\pi a^3}{3} (\rho_1 - \rho_0) gy, \quad (14)$$

where $g = 9.8 \text{ m/s}^2$ is the Earth gravity acceleration.

4. Microdroplet dynamics

The microdroplet dynamics is computed considering the dynamic viscosity of water $\mu_0 = 10^{-3} \text{ Pa} \cdot \text{s}$. Let \mathbf{r} and $\dot{\mathbf{r}} = d\mathbf{r}/dt$ denote, respectively, the position and the velocity of a microdroplet at the time t . The flow around the microdroplet is assumed to be laminar. Hence, the drag force on the microdroplet is given by the Stokes' law [32] $\mathbf{F}^{\text{drag}} = 6\pi\mu_0 a \dot{\mathbf{r}}$. According to Newton's second law, the microdroplet position is described by the differential equation

$$\ddot{\mathbf{r}} + \gamma \dot{\mathbf{r}} = \mathbf{a}^{\text{rad}}(\mathbf{r}) + \mathbf{g}^{\text{eff}}, \quad (15)$$

where $\gamma = 9\mu_0/(2a^2\rho_1)$ is viscous damping coefficient, $\mathbf{a}^{\text{rad}} = 3\mathbf{F}^{\text{rad}}/(4\pi a^3\rho_1)$ is the acceleration due to the radiation force, and $\mathbf{g}^{\text{eff}} = (\rho_0/\rho_1 - 1)g\mathbf{e}_y$ is the acceleration due to gravity and buoyancy effects, with \mathbf{e}_y being the unit-vector along the y-axis. Equation (15) was solved using the forth-order Runge-Kutta method in MATLAB (The MathWorks Inc., Natick MA, USA).

The particle dynamics discussed here neglects acoustic streaming caused by nonlinear and absorption effects in the host medium. In fact, acoustic streaming may affect entrapment owing to the fact that it may cause an additional drag force on the trapped particle. However, a study found that acoustic streaming by a focused source is more significant in the focal and post-focal regions [33].

5. Numerical results and discussion

Consider the host medium as water with the following physical parameter $\rho_0 = 1000 \text{ kg/m}^3$, $c_0 = 1480 \text{ m/s}$, and $\nu_0 = 10^{-6} \text{ m}^2/\text{s}$. The circular focused transducer used to generate the incident ultrasound beam to the microdroplets operates at

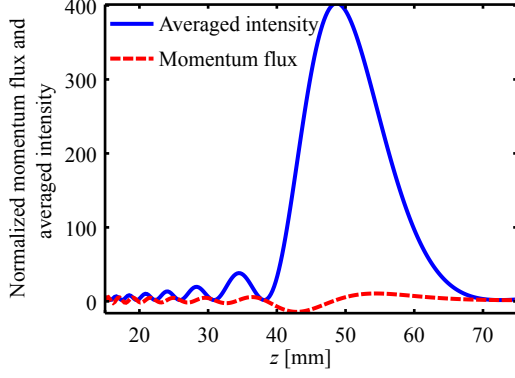


Figure 2: (Color online) Normalized time-averaged intensity \bar{I}/I_0 and normalized momentum flux divergence $k^{-1}c_0\text{Im}[\nabla \cdot \rho_0 \mathbf{v}_{\text{in}} \mathbf{v}_{\text{in}}^*]/I_0$ along the z -axis, produced by the focused transducer operating at 1 MHz frequency.

1 MHz with intensity $I_0 = \rho_0 c_0 v_0^2/2 = 3.3 \text{ kW/m}^2$. At this frequency, the external viscous boundary around the microdroplet is $\delta_0 = 0.56 \mu\text{m}$. The transducer has aperture $2b = 40 \text{ mm}$, focal distance $z_0 = 50 \text{ mm}$, and an f -number $N = 1.25$. Since $kb = 84.9$ and $N = 1.25$, the paraxial approximation inequalities in (2) are readily satisfied. Two types of microdroplets of radii $a = 58.9 \mu\text{m}$ and size parameter $ka = 0.25$ (Rayleigh particles) made of benzene and peanut oil are considered for trapping. Note that the microdroplets are immiscible in water. At room temperature, the physical parameters for benzene are [40] $\rho_1 = 870 \text{ kg/m}^3$, $c_1 = 1295 \text{ m/s}$, $f_0 = -0.5$, $f_1 = -0.09$, $v_1 = 7.47 \times 10^{-7} \text{ m}^2/\text{s}$, $\delta_1 = 0.46 \mu\text{m}$, and $\alpha_1 = 8.73 \times 10^{-13} \text{ Np MHz}^{-2} \text{ m}^{-1}$; while for peanut oil we have [41] $\rho_1 = 913 \text{ kg/m}^3$, $c_1 = 1465.9 \text{ m/s}$, $f_0 = -0.12$, $f_1 = -0.06$, $v_1 = 8.1 \times 10^{-5} \text{ m}^2/\text{s}$, $\delta_1 = 5 \mu\text{m}$, and $\alpha_1 = 1.5 \times 10^{-12} \text{ Np MHz}^{-2} \text{ m}^{-1}$. With these parameters, the external and the internal viscous boundary layers of the microdroplets satisfy $\delta_0 \ll a$ and $\delta_1 \leq a/6$, respectively.

5.1. Paraxial approximation model

In Fig. 2, we show the normalized momentum flux divergence $k^{-1}c_0\text{Im}[\nabla \cdot \rho_0 \mathbf{v}_{\text{in}} \mathbf{v}_{\text{in}}^*]/I_0$ and the normalized time-averaged intensity \bar{I}/I_0 along the z -axis. These quantities were computed using Eqs. (A.4) and (A.5). Within the range $0.3z_0 < z < 1.5z_0$, the amplitude of the normalized momentum flux is less than 10% of that due to the normalized time-averaged intensity. Therefore, we may neglect the contributions of the momentum flux divergence term in both scattering and absorption radiation forces given in Eqs. (10) and (11), respectively.

The axial radiation force components acting on a benzene and a peanut oil microdroplet are shown in Fig. 3. The radiation components were computed using Eqs. (8)-(11). The gray region corresponds to the pre-focal zone of the transducer. A trapping point is determined by observing that the radiation force has negative slope and changes sign as a particle passes through it. It is clear that the benzene microdroplet can be axially trapped at the focal distance $z_0 = 50 \text{ mm}$. Nevertheless, this is not the case for the peanut oil microdroplet, because the absorption radiation force is greater than of the magnitude of the minimum value of the gradient force.

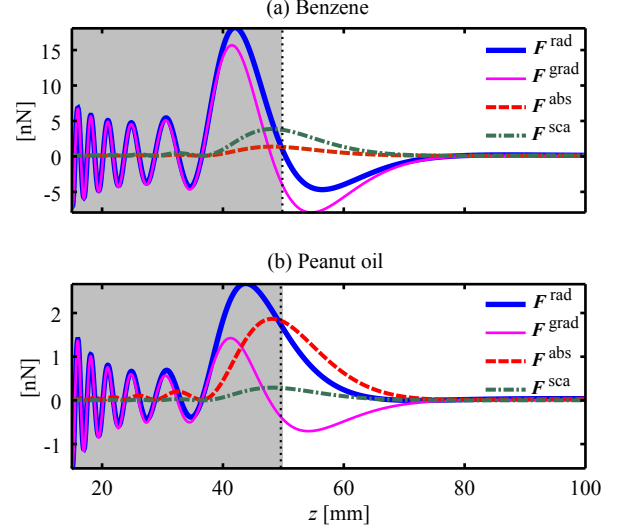


Figure 3: (Color online) Axial radiation force components produced by the focused transducer on (a) a benzene and (b) a peanut oil microdroplet with size parameter $ka = 0.25$ and suspended in water. The transducer operates at 1 MHz with intensity $I_0 = 3.3 \text{ kW/m}^2$. The radiation components were computed using Eqs. (8)-(11). The region in gray depicts the transducer pre-focal zone $z < z_0 = 50 \text{ mm}$.

In Fig. 4, the axial and transverse radiation forces exerted on the microdroplets are illustrated in the transducer pre-focal zone $z < z_0 = 50 \text{ mm}$. Five trapping points, marked with gray dots, are recognized in the pre-focal zone at $z = 16.5, 18.8, 21.8, 26.1, 32.6 \text{ mm}$. It should be noticed that off-axial stable points are also present in the transducer pre-focal region.

In Fig. 5, we show the radiation force potential U^{rad} along the z -axis in the transducer pre-focal zone $z < z_0 = 50 \text{ mm}$. The potential was calculated using Eq. (9). Five stable trapping points are noticed in the minima of the potential function.

The effective potential energy U^{eff} along the y -axis of both microdroplets are depicted in Fig. 6. Clearly, potential wells are formed for all trapping points observed in Fig. 4. Thus, they are points of stable equilibrium. The negative slope observed in the effective energy potential as y increases appears because we considered gravity effects as described in Eq. (14). If the microdroplet mechanical energy lies within the potential well, then the microdroplet will oscillate around the minimum of U^{eff} . Due to the host fluid viscosity the mechanical energy is worn out and the microdroplet is eventually trapped. For the benzene microdroplet, the width of the potential well is about $50a$ (where a is the microdroplet radius) at $z = 32.6 \text{ mm}$, but it becomes $25a$ at $z = 16.5 \text{ mm}$. The width of the potential well for the oil droplet is $26a$ at $z = 33 \text{ mm}$, whereas it becomes $16a$ at $z = 16.5 \text{ mm}$. The obtained width of the potential wells suggests that many microparticles can be held on the same trapping point. Moreover, Figs. 5 and 6 show that the considered microdroplets can be three-dimensionally trapped in the medium.

5.2. Microdroplet dynamics

The trajectories in phase space of the microdroplets are displayed in Fig. 7. The initial position of the benzene

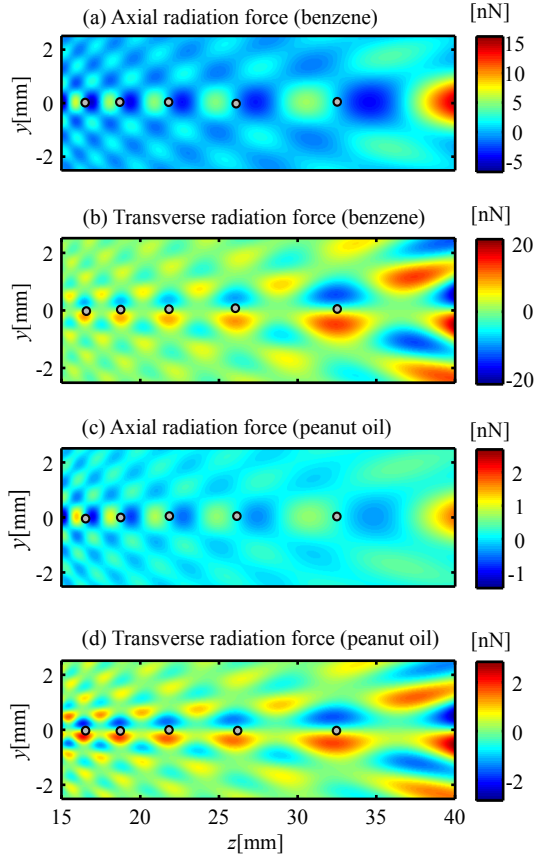


Figure 4: (Color online) The acoustic radiation force (axial and transverse) produced by the focused transducer on (a) and (b) the benzene, and (c) and (d) the oil microdroplets with size parameter $ka = 0.25$ in water. The transducer operates at 1 MHz with intensity $I_0 = 3.3 \text{ kW/m}^2$. Gray dots indicate axial trapping points at $z = 16.5, 18.8, 21.8, 26.1, 32.6 \text{ mm}$. The acoustic radiation force was computed using Eqs. (8)-(11).

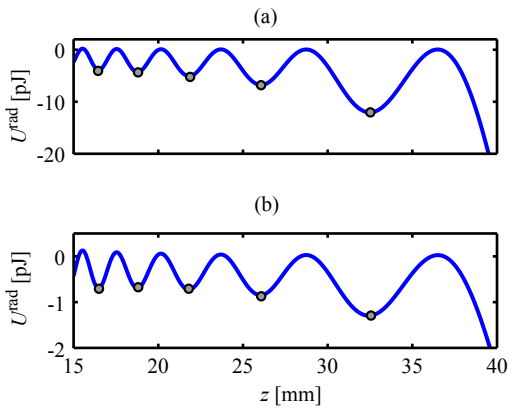


Figure 5: (Color online) Radiation force energy potential in the pre-focal zone $z < z_0 = 50 \text{ mm}$ generated by the focused transducer for (a) a benzene and (b) a peanut oil microdroplet with size parameter $ka = 0.25$ and suspended in water. The transducer operates at 1 MHz with intensity $I_0 = 3.3 \text{ kW/m}^2$. The potential was computed using Eq. (9). The gray dots indicate the stable trapping points at $z = 16.5, 18.8, 21.8, 26.1, 32.6 \text{ mm}$.

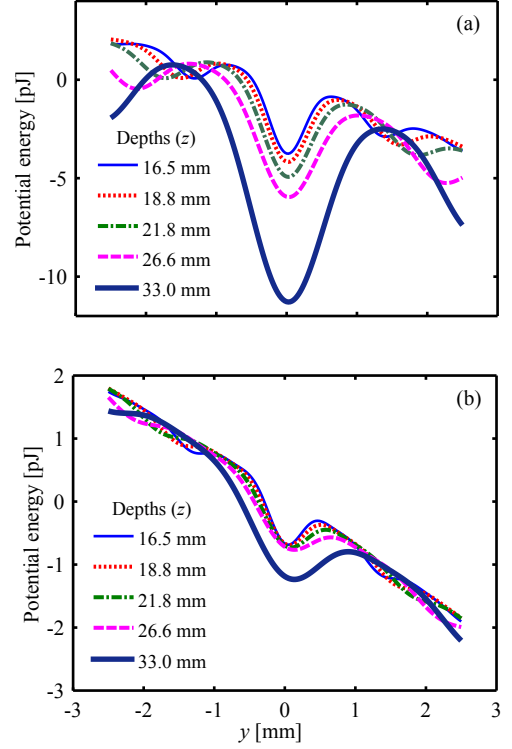


Figure 6: (Color online) Effective potential energy U^{eff} along the y -axis of (a) a benzene and (b) an oil microdroplets with size parameter $ka = 0.25$ and suspended in water. The transducer operates at 1 MHz with intensity $I_0 = 3.3 \text{ kW/m}^2$. The potential functions were computed using Eq. (9) at different depths corresponding to the gray dots in Fig. 5.

and oil microdroplets are, respectively, $(0.1, 0.1, 16.1) \text{ mm}$ and $(0.1, 0.1, 26.0) \text{ mm}$, with zero initial velocity. According to Fig. 4, the nearest trapping points to the microdroplets initial positions are $z_1 = 16.5 \text{ mm}$ and $z_2 = 26.2 \text{ mm}$. It is worthy to note that the microdroplets dynamics is similar to a damped harmonic oscillator, with a characteristic decaying time (i.e. 5% of the maximum displacement) of about 6 s. Beyond the decaying time, the microdroplets are three-dimensionally trapped. Referring to Fig. 6, it is noticeable that the chosen trapping points have the shallowest potential wells in the pre-focal zone. Even so, entrapment occurs. Therefore, one should expect that the microdroplet will be held in all other trapping points, since their associated potential wells are deeper than those chosen here. Moreover, the particle dynamics in the x and the y directions are different because gravity and buoyancy breaks the spatial symmetry of the radiation force potential U^{rad} .

5.3. Finite element method

Here we compared the radiation force results obtained in the paraxial approximation as given in Eq. (4), with computational simulations based on the finite element method (FEM). The acoustic fields yielded by the circular focused transducer driven at 1 MHz with intensity 3.3 kW/m^2 was simulated in COMSOL Multiphysics (Comsol Inc., Burlington, MA USA). The perfect matched layer (PML) boundary condition was employed on the edges of the simulation domain, to avoid spurious wave reflections back into the medium.

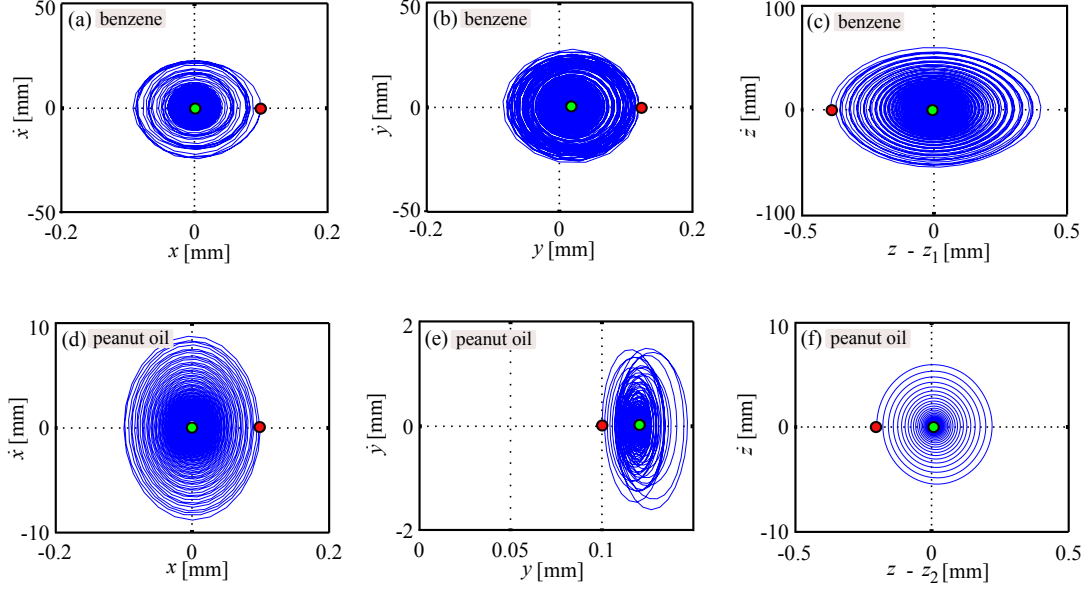


Figure 7: (Color online) The trajectories in phase space of (a)-(c) the benzene and (d)-(f) peanut oil microdroplets suspended in water and under the effective potential U^{eff} given in Eq. (14). The trapping point depths are, respectively, at $z_1 = 16.5$ mm and $z_2 = 26.2$ mm. The red and the green dots indicate the initial and final coordinates of the microdroplet, respectively.

In Fig. 8, we show the pressure generated by the transducer in the FEM simulation. The region describing water is formed by a triangular mesh having 8 triangles per wavelength. The simulation convergence was verified by computing the spatially averaged pressure in a rectangular region of 4×20 mm and centered in the transducer focus point. No significant change in the averaged pressure was observed by setting the number of triangles per wavelength larger than 4.

Because the acoustic radiation force in the transducer pre-focal zone is mostly due to the gradient force, we computed the radiation force potential U^{rad} of an oil microdroplet using Eq. (9) for both paraxial approximation and finite element methods. In Fig. 9, we show the radiation force potential along the z -axis. In the region between 15 and 40 mm, the FEM simulation revealed four stable trapping points labeled as P_1, P_2, P_3 , and P_4 at, respectively, $z = 32.6, 25.7, 20.9, 17.2$ mm. Points P_1 and P_2 coincide to those predicted by the paraxial approximation method. Nonetheless the methods yield different locations for points P_3 and P_4 . The discrepancy between the two methods seen here is somehow expected since the paraxial approximation yields an unreliable solution in a region from $z = 0$ to approximately 30% of the transducer focal distance [34]. In addition, the FEM simulations predict a total of nine axial trapping points in the pre-focal region.

6. Summary and conclusions

The concept of multitrapping acoustical tweezer based on a single focused ultrasound beam provides a simple method for simultaneous manipulation of microparticles (Rayleigh particles). By performing computational simulations based on the paraxial approximation method, it has been demonstrated that a focused piezoelectric transducer operating at 1 MHz with an

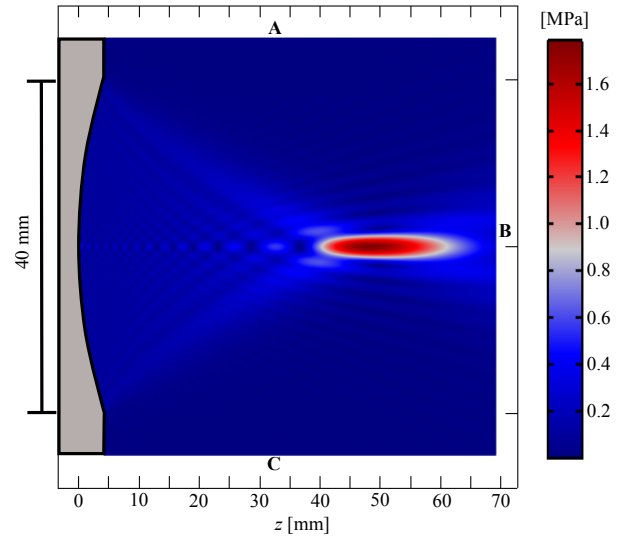


Figure 8: (Color online) Acoustic pressure produced by the circular focused transducer with aperture $2b = 40$ mm, focus at $z_0 = 50$ mm, 1 MHz frequency, and intensity of $I_0 = 3.3$ kW/m², operating in water at room temperature. The pressure is obtained through computational simulations based on the finite element method with perfect matched layer boundary conditions on the domain edges labeled as A, B, and C. The transducer is mounted on a rigid-baffle in which the fluid velocity is assumed to be zero.

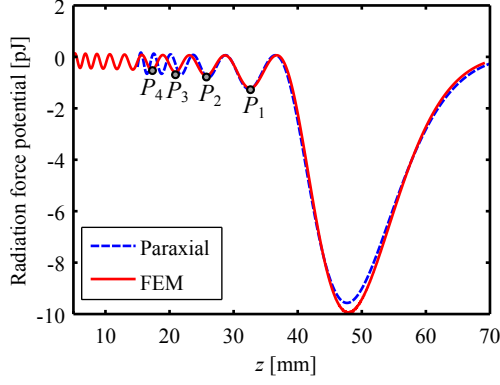


Figure 9: (Color online) The radiation force potential U^{rad} of a peanut oil droplet of size parameter $ka = 0.25$, obtained with the paraxial approximation and the finite-element methods. The points labeled as P_i ($i = 1, 2, 3, 4$) are located, respectively, at $z = 32.6, 25.7, 20.9, 17.2$ mm.

intensity of 3.3 kW/m^2 can axially trap microdroplets in the transducer pre-focal zone. The trapping radiation force is in the nanonewtons range. We can further notice in Fig. 4 that off-axis stable points are also present in the pre-focal region.

Unlike entrapment in the focal region, the stability of traps in the pre-focal zone is not affected by the absorption and the scattering radiation forces. In principle, any less dense and more compressible microdroplet with respect to the host liquid can be trapped in the pre-focal zone of the transducer. Moreover, numerical simulations of the particle dynamics in a viscous fluid have shown that the microdroplets are indeed trapped in the pre-focal zone. We emphasize that these results depends on the paraxial approximation used to derive the acoustic fields generated by the transducer.

A numerical simulation of the wave pressure generated by the focused transducer was performed based on the finite element method (FEM). After calculating the gradient force on an oil microdroplet, we also found axial trapping points in the pre-focal region. The methods have good agreement in the region $z > 20$ mm.

If experimental investigations confirm the theoretical predictions exposed here, the proposed method might be an advance in microparticle handling devices based on piezoelectric transducers.

Appendix A. Axial momentum flux and time-averaged intensity

Let us analyze the divergence of the momentum flux $\text{Im}[\nabla \cdot \rho_0 \mathbf{v}_{\text{in}} \mathbf{v}_{\text{in}}^*]$ in Eqs. (10) and (11). Since the paraxial beam described in Eq. (4) is axisymmetric, the azimuthal component of the fluid element velocity is zero, $v_{\text{in},\varphi} = 0$. Hence, the divergence of the momentum flux term (second-rank tensor) of an

axisymmetric beam, in cylindrical coordinates, is given by [42]

$$\begin{aligned} \nabla \cdot \rho_0 \mathbf{v}_{\text{in}} \mathbf{v}_{\text{in}}^* = & \rho_0 \left[\left[\partial_{\varrho} (v_{\text{in},\varrho} v_{\text{in},\varrho}^*) + \partial_z (v_{\text{in},\varrho} v_{\text{in},z}^*) + \frac{v_{\text{in},\varrho} v_{\text{in},\varrho}^*}{\varrho} \right] \mathbf{e}_{\varrho} \right. \\ & \left. + \left[\partial_{\varrho} (v_{\text{in},\varrho} v_{\text{in},z}^*) + \frac{v_{\text{in},\varrho} v_{\text{in},z}^*}{\varrho} + \partial_z (v_{\text{in},z} v_{\text{in},z}^*) \right] \mathbf{e}_z \right]. \end{aligned} \quad (\text{A.1})$$

By taking the imaginary-part of this expression, we get

$$\text{Im}[\nabla \cdot \rho_0 \mathbf{v}_{\text{in}} \mathbf{v}_{\text{in}}^*] = \rho_0 \left[\partial_z (v_{\text{in},\varrho} v_{\text{in},z}^*) \mathbf{e}_{\varrho} + \left[\partial_{\varrho} (v_{\text{in},\varrho} v_{\text{in},z}^*) + \frac{v_{\text{in},\varrho} v_{\text{in},z}^*}{r} \right] \mathbf{e}_z \right]. \quad (\text{A.2})$$

Referring to Eq. (6) and considering $\varrho = 0$, we find that the transverse component of the fluid element velocity is $v_{\text{in},\varrho}(0, z) = 0$. Thus, in the axial direction Eq. (A.2) becomes

$$\text{Im}[\nabla \cdot \rho_0 \mathbf{v}_{\text{in}} \mathbf{v}_{\text{in}}^*(0, z)] = \text{Im}[\partial_z (v_{\text{in},z} v_{\text{in},z}^*)]_{\varrho=0} \mathbf{e}_z. \quad (\text{A.3})$$

With aid of MATHEMATICA software [43] and using Eq. (6), we obtain

$$\begin{aligned} \text{Im}[\nabla \cdot \rho_0 \mathbf{v}_{\text{in}} \mathbf{v}_{\text{in}}^*(0, z)] = & \frac{\rho_0 v_0^2 z_0^2}{2z^2(z-z_0)^3} \left[8z^2 \sin^2 \left[\frac{kb^2(z-z_0)}{4zz_0} \right] \right. \\ & \left. - kb^2(z-z_0) \sin \left[\frac{kb^2(z-z_0)}{2zz_0} \right] \right] \mathbf{e}_z. \end{aligned} \quad (\text{A.4})$$

Another important quantity in the radiation force analysis is the axial time-averaged intensity, which is given for the focused ultrasound beam by

$$\begin{aligned} \bar{I}(0, z) = & \frac{1}{2} \text{Re}[p_{\text{in}}(0, z) v_{\text{in},z}^*(0, z)] \mathbf{e}_z \\ = & \frac{\rho_0 v_0^2 c_0}{2} \frac{(4z^2 - b^2) z_0^2}{z^2(z-z_0)^2} \sin^2 \left[\frac{kb^2(z-z_0)}{4zz_0} \right] \mathbf{e}_z. \end{aligned} \quad (\text{A.5})$$

Acknowledgements

This work was partially supported by grants 481284/2012-5 and 303783/2013-3 CNPq (Brazilian agency).

References

References

- [1] A. Ashkin, Acceleration and trapping of particles by radiation pressure, *Phys. Rev. Lett.* 24 (1970) 156–159.
- [2] G. R. Torr, The acoustic radiation force, *Am. J. Phys.* 52 (1984) 402–408.
- [3] D. G. Grier, A revolution in optical manipulation, *Nature* 424 (6950) (2003) 810–816.
- [4] T. Laurell, F. Petersson, A. Nilsson, Chip integrated strategies for acoustic separation and manipulation of cells and particles, *Chem. Soc. Rev.* 36 (2007) 492–506.
- [5] J. Friend, L. Y. Yeo, Microscale acoustofluidics: Microfluidics driven via acoustics and ultrasonics, *Rev. Mod. Phys.* 83 (2011) 647–704.
- [6] X. Ding *et al.*, On-chip manipulation of single microparticles, cells, and organisms using surface acoustic waves, *Proc. Natl. Acad. Sci. U.S.A* 109 (2012) 11105–11109.
- [7] Y. Li, J. Y. Hwang, K. K. Shung, J. Lee, Single-beam acoustic tweezers: a new tool for microparticle manipulation, *Acou. Today* 9 (2013) 10–13.

- [8] A. Ashkin, J. M. Dziedzic, J. E. Bjorkholm, S. Chu, Observation of a single-beam gradient force optical trap for dielectric particles, *Opt. Lett.* 11 (1986) 288–290.
- [9] J. Wu, Acoustical tweezers, *J. Acoust. Soc. Am.* 89 (1991) 2140.
- [10] K. C. Neuman, E. H. Chadd, G. F. Liou, K. Bergman, S. M. Block, Characterization of photodamage to *Escherichia coli* in optical traps, *Biophys. J.* 77 (1999) 2856–2863.
- [11] T. Kozuka, T. Tuziuti, H. Mitome, T. Fukuda, Control of a standing wave field using a line-focused transducer for two-dimensional manipulation of particles, *Jpn. J. Appl. Phys.* 37 (1998) 2974–2978.
- [12] M. Evander, J. Nilsson, *Acoustofluidics 20: Applications in acoustic trapping*, *Lab Chip*, 12 (2012) 4667–4676.
- [13] P. Glynne-Jones, R. J. Boltryk, M. Hill, *Acoustofluidics 9: Modelling and applications of planar resonant devices for acoustic particle manipulation*, *Lab. Chip* 12 (8) (2012) 1417–1426.
- [14] J. Shi, D. Ahmed, X. Mao, S.-C. S. Lin, A. Lawit, T. J. Huang, Acoustic tweezers: patterning cells and microparticles using standing surface acoustic waves (SSAW), *Lab. Chip* 9 (2009) 2890–2895.
- [15] S. B. Q. Tran, P. Marmottant, P. Thibault, Fast acoustic tweezers for the two-dimensional manipulation of individual particles in microfluidic channels, *Appl. Phys. Lett.* 101 (2012) 114103.
- [16] C. R. P. Courtney, C. E. M. Demore, H. Wu, A. Grinenko, P. D. Wilcox, S. Cochran, B. W. Drinkwater, Independent trapping and manipulation of microparticles using dexterous acoustic tweezers, *Appl. Phys. Lett.* 104 (2014) 154103.
- [17] J. Meng, D. Mei, K. Jia, Z. Fan, Y. K. Contactless and non-invasive delivery of micro-particles lying on a non-customized rigid surface by using acoustic radiation force, *Ultrasonics* 54 (2014) 1350–1357.
- [18] D. Foresti, M. Nabavi, M. Klingauf, A. Ferrari, D. Poulikakos, Acoustophoretic contactless transport and handling of matter in air, *Proc. Natl. Acad. Sci. U. S. A.* 110 (2013) 12549.
- [19] D. Foresti, D. Poulikakos, Acoustophoretic contactless elevation, orbital transport and spinning of matter in air, *Phys. Rev. Lett.* 112 (2014) 024301.
- [20] J. Lee, S.-Y. Teh, A. Lee, H. H. Kim, C. Lee, K. K. Shung, Single beam acoustic trapping, *Appl. Phys. Lett.* 95 (2009) 073701.
- [21] J. Lee *et al.*, Targeted cell immobilization by ultrasound microbeam, *Biotechnol. Bioeng.* 108 (2011) 1643–1650.
- [22] K. H. Lam *et al.*, Ultrahigh frequency lensless ultrasonic transducers for acoustic tweezers application, *Biotechnol. Bioeng.* 110 (2013) 881–886.
- [23] Y. Choe, J. W. Kim, K. K. Shung, E. S. Kim, Microparticle trapping in an ultrasonic Bessel beam, *Appl. Phys. Lett.* 99 (2011) 233704.
- [24] H.-S. Hsu *et al.*, Focused high frequency needle transducer for ultrasonic imaging and trapping, *Appl. Phys. Lett.* 101 (2012) 024105.
- [25] F. Zheng *et al.*, Acoustic trapping with a high frequency linear phased array, *Appl. Phys. Lett.* 101 (2012) 214104.
- [26] J. Wu, G. Du, Acoustic radiation force on a small compressible sphere in a focused beam, *J. Acoust. Soc. Am.* 87 (1990) 997–1003.
- [27] X. Chen, R. E. Apfel, Radiation force on a spherical object in an axisymmetric wave field and its application to the calibration of high-frequency transducers, *J. Acoust. Soc. Am.* 99 (1996) 713–724.
- [28] D. Baresch, J.-L. Thomas, R. Marchiano, Spherical vortex beams of high radial degree for enhanced single-beam tweezers, *J. Appl. Phys.* 113 (2013) 184901.
- [29] O. A. Sapozhnikov, M. R. Bailey, Radiation force of an arbitrary acoustic beam on an elastic sphere in a fluid, *J. Acoust. Soc. Am.* 133 (2013) 661–676.
- [30] F. G. Mitri, Near-field single tractor-beam acoustical tweezers, *Appl. Phys. Lett.* 103 (2013) 114102.
- [31] A. D. Pierce, *Acoustics: An Introduction to Its Physical Principles and Applications*, Acoustical Society of America, Melville, NY, 1989, p. 234.
- [32] L. D. Landau, E. M. Lifshitz, *Fluid Mechanics*, 2nd Edition, Vol. 6, Course of Theoretical Physics, Pergamon Press, Oxford, 1993.
- [33] T. Kamakura and K. Matsuda and Y. Kumamoto and M. A. Breazeale, Acoustic streaming induced in focused Gaussian beams, *J. Acoust. Soc. Am.* 97 (1995) 2740–2746.
- [34] B. G. Lucas, T. G. Muir, The field of a focusing source, *J. Acoust. Soc. Am.* 72 (1982) 1289–1296.
- [35] F. G. Mitri, High-order pseudo-Gaussian scalar acoustical beams, *IEEE Trans. Ultras. Ferroel. Freq. Control* 61 (2014) 191–196.
- [36] G. T. Silva, An expression for the radiation force exerted by an acoustic beam with arbitrary wavefront (L), *J. Acoust. Soc. Am.* 130 (2011) 3541–3544.
- [37] G. T. Silva, Acoustic radiation force and torque on an absorbing compressible particle in an inviscid fluid, *J. Acoust. Soc. Am.* (2014) in press.
- [38] L. P. Gorkov, On the forces acting on a small particle in an acoustic field in an ideal fluid, *Sov. Phys. Dokl.* 6 (1962) 773–775.
- [39] P. S. Epstein, R. Carhart, The absorption of sound in suspensions and emulsions. I. Water fog in air, *J. Acoust. Soc. Am.* 25 (1953) 553–565.
- [40] G. S. Kino, *Acoustic Waves: Devices, Imaging, and Analog Signal Processing*, Prentice-Hall, Upper Saddle River, New Jersey, USA, 1987, p. 548.
- [41] J. N. Coupland, D. J. McClements, Physical properties of liquid edible oils, *J. Am. Oil Chem. Soc.* 12 (1997) 1559–1564.
- [42] L. P. Lebedev, M. J. Cloud, V. A. Eremeyev, *Tensor Analysis with Applications in Mechanics*, World Scientific Publishing, Singapore, 2010, p. 111.
- [43] Wolfram Research, Inc., *Mathematica*, Ver. 10.0, Champaign, IL USA, 2014.